



Full length article

Morphology evolution and nanostructure of chemical looping transition metal oxide materials upon redox processes

Lang Qin ^{a,1}, Zhuo Cheng ^{a,1}, Mengqing Guo ^{a,1}, Jonathan A. Fan ^b, Liang-Shih Fan ^{a,*}^a Department of Chemical and Biomolecular Engineering, The Ohio State University, 140 West 19th Ave, Columbus, OH 43210, USA^b Department of Electrical Engineering, Ginzton Laboratory, Spilker Engineering and Applied Sciences, 348 Via Pueblo Mall, Stanford University, Stanford, CA 94305, USA

ARTICLE INFO

Article history:

Received 18 May 2016

Received in revised form

6 October 2016

Accepted 8 November 2016

Available online 24 November 2016

Keywords:

Chemical looping

Transition metal

Redox reaction

ABSTRACT

Transition metal are heavily used in chemical looping technologies because of their high oxygen carrying capacity and high thermal reactivity. These oxygen activities result in the oxide formation and oxygen vacancy formation that affect the nanoscale crystal phase and morphology within these materials and their subsequent bulk chemical behavior. In this study, two selected earlier transition metals manganese and cobalt as well as two selected later transition metals copper and nickel that are important to chemical looping reactions are investigated when they undergo cyclic redox reactions. We found Co microparticles exhibited increased CoO impurity presence when oxidized to Co₃O₄ upon cyclic oxidation; CuO redox cycles prefer to be limited to a reduced form of Cu₂O and an oxidized form of CuO; Mn microparticles were oxidized to a mixed phases of MnO and Mn₃O₄, which causes delamination during oxidation. For Ni microparticles, a dense surface were observed during the redox reaction. The atomistic thermodynamics methods and density functional theory (DFT) calculations are carried out to elucidate the effect of oxygen dissociation and migration on the morphological evolution of nanostructures during the redox processes. Our results indicate that the earlier transition metals (Mn and Co) tend to have stronger interaction with O₂ than the later transition metals (Ni and Cu). Also, our modified Brønsted–Evans–Polanyi (BEP) relationship for reaction energies and total reaction barriers reveals that reactions of earlier transition metals are more exergonic and have lower oxygen dissociation barriers than those of later transition metals. In addition, it was found that for these transition metal oxides the oxygen vacancy formation energies increase with the depth. The oxide in the higher oxidation state of transition metal has lower vacancy formation energy, which can facilitate forming the defective nanostructures. The fundamental understanding of these metal oxide reactions is essential to designing the metal oxide-based oxygen carriers for chemical looping applications.

© 2016 Acta Materialia Inc. Published by Elsevier Ltd. All rights reserved.

1. Introduction

Chemical looping is regarded as one of the most cost effective technique [1] for clean conversion of carbonaceous fuels along with CO₂ capture [2]. In the past few decades, application of metal oxides in clean energy industry attracts numerous attentions. In particular, chemical looping requires highly efficient materials with low cost and high performance and durability. Transition metal oxides are among the most promising candidates, exhibiting a wide range of interesting physical and chemical properties. Clean energy can be

harvested by chemical looping system from carbonaceous fuels [3]. The metal oxide composites play a key role as oxygen carriers and can be operated under various modes. In the chemical looping combustion (CLC) mode, the oxygen carriers react with fuels and are completely re-oxidized in a combustor, thus the whole combustion processes produce only heat. The chemical looping oxygen uncoupling (CLOU) process mode is based on CLC with metal oxides releasing gaseous oxygen to convert carbonaceous fuels. In both of these chemical looping modes of operation, the diffusion of metal ions, oxygen ions, and oxygen vacancies dictates the redox reactivity and recyclability of the metal oxide oxygen carriers [4].

The state of the art study on metal oxides in chemical looping application largely focus on the selection of materials using trial and error method and the relationship between morphology or

* Corresponding author.

E-mail address: fan.1@osu.edu (J.A. Fan).¹ These authors contributed equally to this work.

structure and reactions have yet been studied systematically. In previous study, we have discussed the reaction mechanism of iron based metal oxide composites at atomic level [4,5]. When supported by titanium oxide, the iron oxide oxygen carriers perform outstandingly in CLC application. Other transition metal oxide systems [5–9] have been discussed in CLC and CLOU because of their capability for being fully reduced and oxidized for multiple cycles. Based on experimental observation, oxides of manganese and copper have been studied in CLOU applications because they show a combination of reasonably high partial pressure of oxygen at relevant temperatures in addition to an exothermic reaction, which could result in a temperature increase in a reactor [10,11]. Similarly, oxides of cobalt and nickel have been extensively reported as oxygen carriers in CLC due to their high transport capacity [12,13]. However, fundamental redox mechanisms in the above-mentioned oxides are still not fully understood due to the lack of atomic level information on the structure and morphology related properties for these oxides. Specifically, the morphology and structure related reaction mechanism has not been discussed in any of the previous work.

The redox reactivity is intrinsically dependent on morphology, electron and crystal structures in metal oxides oxygen carrier. For example, Fe based oxide composites have been successfully demonstrated to recycle over thousands of times in chemical looping systems with the aid of Ti-based support [14]. This is because of the lower vacancy formation energy of Ti terminated surface compared to Fe terminated surface, which results in the formation of defective surface and large surface area with addition of Ti. Thus, it is critical to understand the oxygen migration and the morphology variation behavior of these materials upon the high temperature oxidation and reduction reactions of metal.

Oxygen vacancies will form with the oxygen migration. For years oxygen vacancies have been examined and investigated by a variety of spectroscopic techniques. Nevertheless, it is still difficulty to experimentally determine the vacancy-induced lattice relaxations, and the vacancy formation energy. A great number of theoretical studies on oxygen migration and vacancy formation from transition metal oxides have been reported, such as TiO_2 [15,16], ZrO_2 [17,18], V_2O_5 [19–21] and CeO_2 [22–25]. However, oxygen migration and vacancy formation in oxides of cobalt, copper, manganese and nickel, used as important chemical looping oxygen carrier materials, still remain unclear.

In this work, we systematically study Co, Cu, Mn and Ni to explore the morphological evolution of the active systems under the redox reactions using the crystal phase study combined with atomic modeling. The comprehensive understanding of the oxygen adsorption, dissociation and diffusion in these metal oxide composites is obtained, which is useful in directing the development of metal oxide-based oxygen carriers for chemical looping applications.

2. Methods

2.1. Experimental

Cu (99%), Ni(99.5+%), Mn(99.5%), Co(99.8%) powders were purchased from Goodfellow. An SEM analysis shows particle sizes between 40 and 60 μm . The powders were washed with acetone three times and dried at room temperature prior to further examination. Approximately 0.1 g powder samples were mounted in an alumina crucible and run through either one oxidation step or between one and five oxidation-reduction cycles at 700 °C using a Setaram SETSYS Evolution Thermogravimetric Analyzer (TGA). Oxidation was performed using a 200 mL/min flow of gas consisting of 50% air balanced with N_2 . The reduction step used a 200 mL/

min flow of gas containing 50% H_2 balanced with N_2 . The oxidation and reduction steps lasted for 30 min each and were alternated with an intermediate 10 min flushing step using N_2 at 100 mL/min. All samples were analyzed using a Rigaku SmartLab X-Ray Diffractometer (XRD) with eliminated fluorescence. Scans were run from 20 to 80° at a rate of 1° per minute with an accelerating voltage and filament current of 40 kV and 44 mA, respectively. All the XRD spectra were analyzed using PDXL software and identified with the JCPDS database.

2.2. Computational

The first-principle calculations were performed within the framework of density functional theory (DFT), using the Vienna Ab Initio Simulation Package (VASP) [26–28]. The generalized gradient approximation of Perdew, Burke and Ernzerhof [29] was used to represent the exchange-correlation energy. The projector-augmented wave (PAW) method [30,31], with a 400 eV energy cutoff, was used to describe the wave functions of the atomic cores. The tetrahedron method with Blöchl corrections [32] was used to set the partial occupancies for the orbitals. The chemisorption of oxygen molecule to surfaces (100) was modeled for Co, Cu, Mn and Ni. Identical surfaces were modeled for the convenience of comparison of intrinsic metal properties and their impact on O=O bond activation. In all cases, the slab models were initially constructed from the optimized lattices. A five-layer periodic slab was constructed along the (100) Miller plane, with a ~15 Å vacuum along the c-axis which ensures negligible interaction between periodic replicas. To achieve excellent numerical accuracy, the real-space cutoff for the calculation of both the oxygen atom and oxygen molecule is increased to 20 Bohr. The binding energy of O_2 is calculated to be 2.88 eV/O atom, while the bond length and vibrational frequency are 1.22 Å and 1530 cm^{-1} , respectively, in agreement with experimental results (the corresponding values are 2.56 eV/atom, 1.21 Å, and 1580 cm^{-1} [33]).

For O_2 adsorption, different starting configurations were considered, including different adsorption sites and various molecular orientations, to help identify the location of the global minimum for the O_2 /Metal system. The adsorption energies of O_2 on transition metals are calculated using the expression as below:

$$E_{ad} = E_{\text{O}_2} + E_M - E_{(\text{O}_2+M)} \quad (1)$$

where E_{O_2} is the energy of the optimized gas phase geometry of O_2 , E_M is the total energy of the respective transition metal surface, and $E_{(\text{O}_2+M)}$ is the total energy of the slab with adsorbed O_2 . Based on this definition, a more positive E_{ad} corresponds to a more stable configuration.

For transition metal oxides, the oxygen vacancy formation energies are calculated based on the following expression:

$$E_f = E_{tot} - E_V - \frac{1}{2}E_{\text{O}_2} \quad (2)$$

In Equation (2), E_{tot} is the total energy of the stoichiometric surface, E_V is the total energy of the reduced surface with one oxygen vacancy, and E_{O_2} is the total energy of the optimized gas phase O_2 .

For O_2 dissociation and diffusion barrier calculations, the climbing-image nudged elastic band (CI-NEB) method was used [34,35]. This method enabled the stationary points to be mapped out along the minimum energy paths and identify transition states for each of the diffusion processes. Because these paths were directed by force projection, the energy was not necessarily consistent with the force being optimized; thus, the force-based

optimizer was chosen to ensure the convergence of the nudged elastic band algorithm.

To take into consideration realistic experimental conditions, the effect of temperature T is included by explicitly taking into account the surrounding gas phase in terms of ab initio atomistic thermodynamics. We previously developed a modified Brønsted–Evans–Polanyi relationship to calculate the activation energy for the elementary steps of metathesis reaction [36]. Here, we extend this method to calculate the activation energy for O_2 dissociation at chemical looping condition as below:

$$E_a(T) = E_{a,DFT} + \alpha(\Delta H_{dis}(T) - \Delta E_{dis,DFT}) \quad (3)$$

where $E_{a,DFT}$ corresponds to the forward activation energy barrier at 0 K, which is obtained from CI-NEB calculations. $\Delta H_{dis}(T)$ is the dissociation enthalpy at finite temperature, which is calculated from the individual enthalpies of the initial state and the final state for the constituent elementary reactions. $\Delta E_{dis,DFT}$ is the difference between the energies of final state and initial state at 0 K. The variable α denotes the relative position of the transition state compared to the initial (i.e., $\alpha = 0$) or final (i.e., $\alpha = 1$) state of the relevant elementary dissociation reaction. It can be obtained by considering which image in the CI-NEB calculations corresponds to the transition state. When the value of α is close to 0, it describes to an initial-like transition state; thus, the activation energy may be kept at the DFT value. When the value of α is close to 1, it

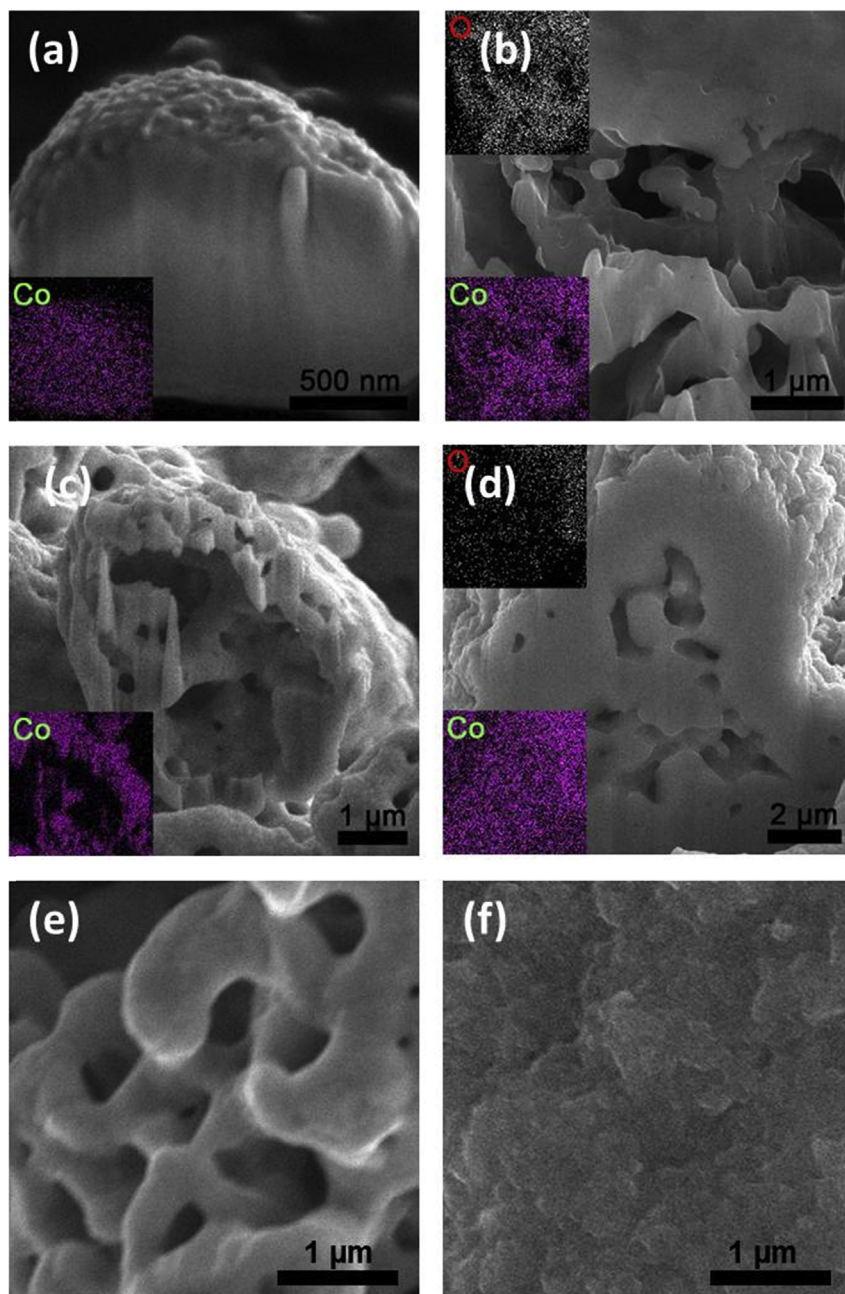


Fig. 1. SEM images of Co microparticles (a) cross section of an initial microparticle; (b) cross section of an oxidized microparticle; (c) cross section of a microparticle after one redox reaction cycle; (d) cross section of a microparticle after five redox reaction cycles; insets: EDS mapping with pink and white representing Co and O, respectively; (e) surface of the microparticle after one redox reaction cycle; (f) surface of the microparticle after five redox reaction cycles. (For interpretation of the references to colour in this figure legend, the reader is referred to the web version of this article.)

corresponds a final-like transition state [37].

3. Results and discussion

3.1. Evolution of nanoscale morphology

The morphology evolution of transition metal microparticles were probed over single and multiple oxidation–reduction cycles at 700 °C. The morphological and structural changes observed are discussed below.

3.1.1. Cobalt

The initial Co microparticles were observed by SEM in Fig. 1(a), the microparticle is dense with an average size of 2 μm. XRD spectrum (Fig. 2 (a)) suggests both fcc (alpha phase) and hcp (beta phase) structures. However, the beta phase only exists in the original microparticles, consequently we mainly consider alpha phase in our DFT calculation during redox reaction to simplify our model.

Particles that have undergone oxidation, on the other hand, experience substantial changes. Here, oxidation results in the formation of a porous microparticle center, as visualized in Fig. 1(b) with Co and O uniformly distributed throughout the microparticle. This is consistent with previous findings [14,38,39] in Fe and FeTi microparticles. These voids in the center reflect that Co atoms initially in the core underwent outward diffusion. Co atoms are ionized during the diffusion process and O ion diffusion occurs mainly through Schottky defects, as opposed to the direct interchange of atoms. A complete phase transformation to Co₃O₄ is shown in Fig. 2(b), suggesting the coexistence of trivalent cobalt and divalent cobalt. Redox cycles were also carried out with the Co microparticles at 700 °C. An SEM image of a particle that had undergone one full redox cycle displays nanopores of 500 nm inside the particle (Fig. 1(c)) and on the surface (Fig. 1(e)). The oxygen vacancies are created during reduction which contributes to nanopore formation. Most of the Co₃O₄ is converted to Co after one redox cycle with a small amount of CoO phase as shown in Fig. 2(c). The quantity of CoO increases dramatically after five redox cycles (Fig. 2(d)). This indicates that the recyclability of microparticles deteriorates due to sintering effects. The decreased surface area and less porous morphology (Fig. 1(d) and (f)) both hinder the mobility of oxygen ions which results in incomplete redox reactions.

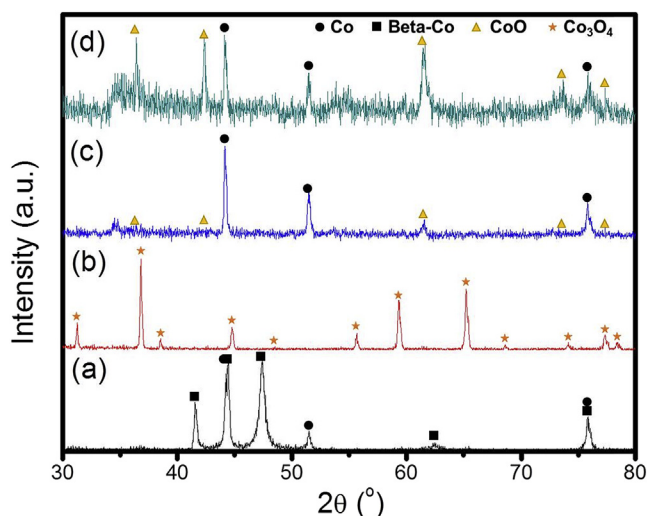


Fig. 2. XRD spectra of Co particle. (a) Initial (b) after oxidation (c) after one redox cycle (d) after five redox cycles at 700 °C.

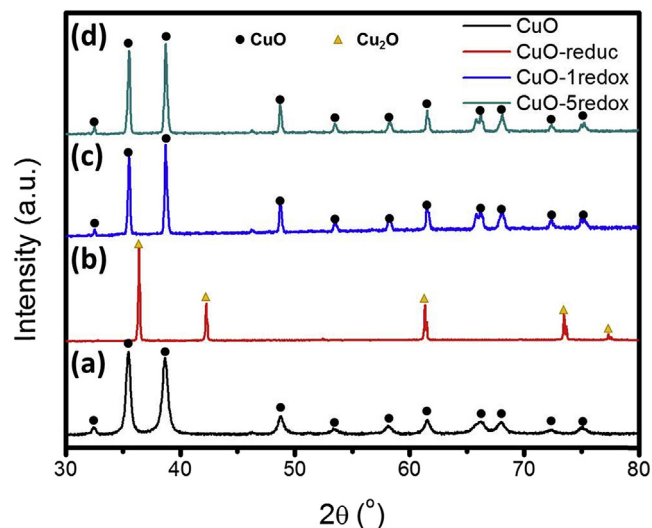
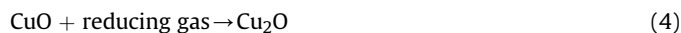


Fig. 3. XRD spectra of CuO microparticles. (a) Initial (b) after reduction (c) after one redox cycle (d) after five redox cycles at 700 °C.

3.1.2. Copper

Cu microparticles were also studied in chemical looping redox reactions for its application in oxygen uncoupling. The low Tamman temperature of Cu (~543 °C) results in a severe sample adherence to the internal wall of TGA sample holder and therefore is not suitable in this study. Consequently, we focus on the fundamentals of CuO in chemical looping oxygen uncoupling (CLOU) application in which the cyclic reactions take place between CuO and Cu₂O.



The excellent recyclability of CuO microparticles is analyzed by XRD in Fig. 3. After cyclic redox reactions the crystal structure of CuO remains unchanged (Fig. 3(c) and (d)). However, based on the XRD analysis, the grain sizes of the microparticles after redox reaction vary substantially. The original average grain size of CuO microparticles is 172 nm, whereas the reduced microparticles has an average grain size of 722 nm and the average size of grains dropped to 400 nm and 365 nm after one and five redox cycles, respectively. This is in agreement with the fact that outward diffusion of oxygen can cause grain expansion. Despite of the sintering effect, the fast kinetics of CuO reduction plays an important role in grain size decrease after redox reactions. Specifically the change in grain size implies a grain boundary movement induced by ionic diffusion during oxygen vacancy exchange. The reduction and oxidation can be treated as creation and consumption of oxygen vacancies, respectively.

3.1.3. Manganese

Initial Mn microparticles are dense as shown in Fig. 4(a) and have a phase pure structure in Fig. 5(a). However, more than one oxidized phase appears during thermal oxidation. MnO and Mn₃O₄ co-exist in the oxidation phases and are both detected by XRD (Fig. 5(b)). The different expansion coefficients of Mn₃O₄ ($8.8 \times 10^{-6}/\text{K}$) [40,41] and MnO ($3.45 \times 10^{-5}/\text{K}$) [42] lead to delamination of the two phases shown in Fig. 4(b). The concentration gradient of oxygen from surface to the core of the microparticle causes an oxygen rich phase shell and a Mn rich core. Consequently, we can speculate that the layer on the surface is

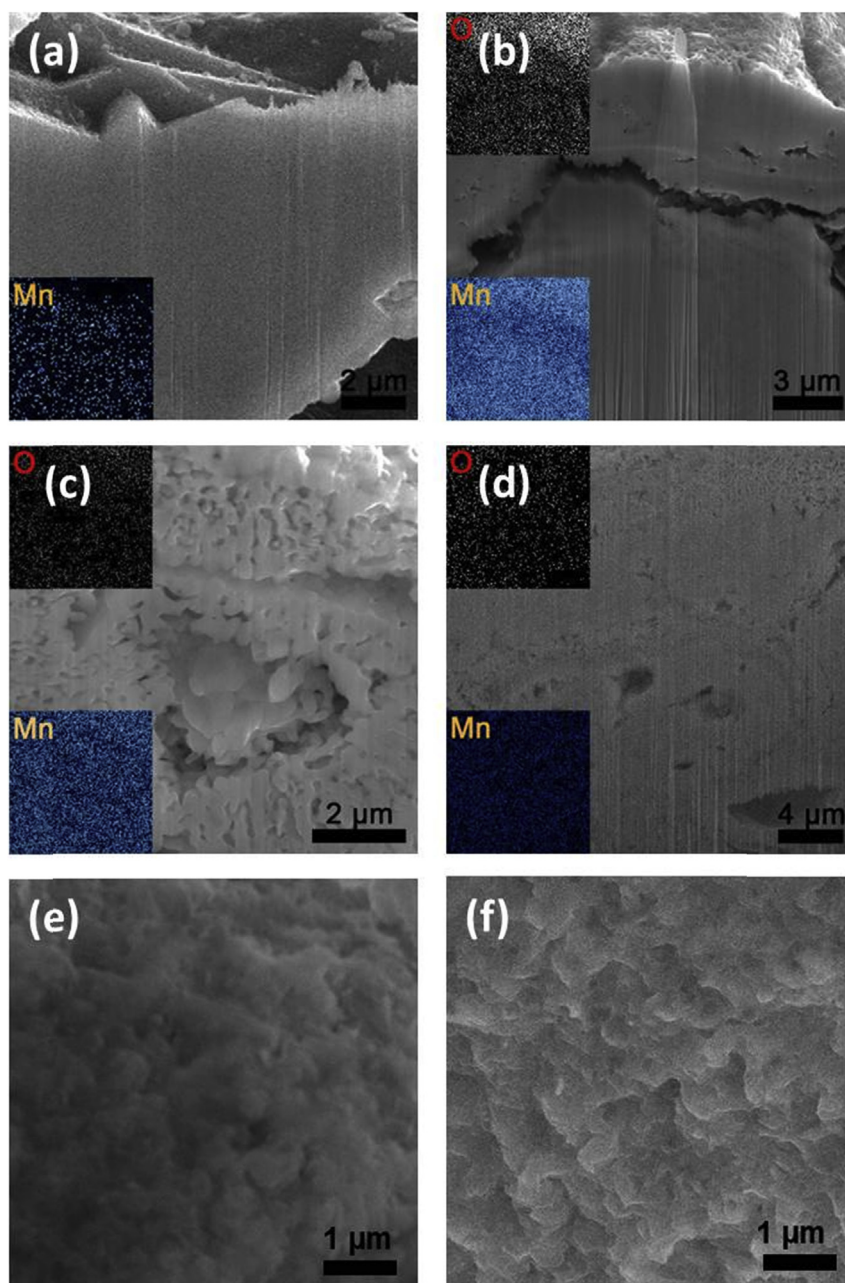


Fig. 4. SEM images of Mn microparticles (a) cross section of an initial microparticle; (b) cross section of an oxidized microparticle; (c) cross section of an microparticle after one redox reaction cycle; (d) cross section of an microparticle after five redox reaction cycles; insets: EDS mapping with blue and white representing Mn and O, respectively; (e) surface of the microparticle after one redox reaction cycle; (f) surface of the microparticle after five redox reaction cycles. (For interpretation of the references to colour in this figure legend, the reader is referred to the web version of this article.)

Mn₃O₄ rich and the inner part of the microparticle is MnO rich. This is confirmed by EDS result in Fig. 4(d), the shell has less X-ray signals generated from Mn than the core. On the other hand, the delamination can be self-healed during the redox reaction. In Fig. 4(c) and (d) clearly show the gap between the shell and core diminishes and disappears, respectively. The self-healing mechanism can be explained: The delamination during oxidation leads to an air filled gap between the shell and core which has a high concentration of oxygen and zero concentration of Mn. Consequently, outward diffusion of oxygen from the core is difficult because of the high to low concentration gradient of oxygen from the gap to the core. This leads to a reducing phase of MnO instead of

Mn in reduction reaction. Meanwhile, sintering effect will promote diffusion of Mn atom at 700 °C, which may fill in the gap after five cycles (Fig. 4(d)). Nevertheless, the delamination during oxidation may weaken mechanical strength of the Mn microparticles and hinders their applications in chemical looping. Moreover, the redox reactions are between MnO and Mn₃O₄, which has less oxygen capacity than looping between Mn and Mn₃O₄.



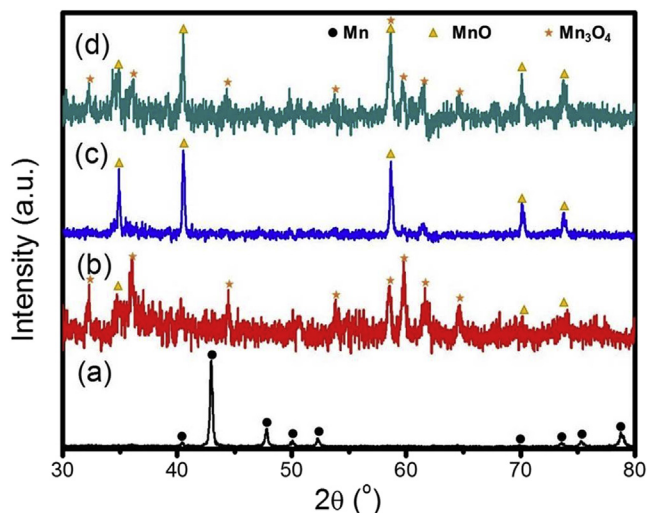


Fig. 5. XRD spectra of Mn particle. (a) Initial (b) after oxidation (c) after one redox cycle (d) after five redox cycles at 700 °C.

3.1.4. Nickel

Ni microparticles are also investigated in this work. The cross sections of an initial Ni microparticle and after reactions remain identical. XRD results (Fig. 7) confirm that the Ni microparticles have little phase and structural change. However, morphology on the surface dramatically changes during the redox reactions. As shown in Fig. 6(b), cubic NiO crystallites form on the surface of oxidized Ni microparticle. Internally, there is little morphological change with few defect incurred dislocations or voids. This suggests the redox reactions take place only on the surface.

3.2. O₂ adsorption on transition metals

To explore the morphological evolution mechanism driven by surface reaction, we first modeled O₂ chemisorption on the transition metal surface, which is the initial step of oxidation of transition metals.

For the O₂/Co(100) system, we label the surface Co atom closest to the oxygen molecule as M1, the Co atom closest to M1 as M2, the Co atom closest to M2 as M3, and the Co atom closest to M3 as M4. The two oxygen atoms are labelled as O1 and O2. Based on this definition, we can describe oxygen adsorption configurations on Co surface. Various adsorption configurations are modeled, optimized and calculated as reported in Table 1. For the considered configurations, the oxygen molecule shows a strong interaction with the Co (001) surface. In the most favorable case, one oxygen atom adsorbs at the M1 site while the other oxygen atom binds to the M3 site as shown in Fig. 8(a), with an adsorption energy of 1.44 eV. The distance between O1 atom and M1 is 2.305 Å, and the distance between O2 atom and M2 is 2.308 Å. An elongation in the O–O distance of adsorbed O₂ may be expected during oxygen activation. In this case, the O–O distance is 0.21 Å larger than the O–O bond of oxygen molecule in gas phase. In the second stable configuration, M1–O1–O2–M2, oxygen molecule is bonded to M1 and M2 site with O–Co bond of 2.411 Å and 2.408 Å, respectively. M2–O1–O2–M4 configuration is found to be 0.19 eV less stable than M1–O1–O2–M3 configuration. The third stable configuration M2–O1–O2–M4 is about 0.61 eV less stable than M1–O1–O2–M3. We also have performed calculations on the perpendicular adsorption of oxygen molecule on one surface Co atom site, but this led to spontaneous

migration of oxygen molecule to form bridging structure.

For the O₂/Cu(100) system, similarly, we label four distinguishable surface Cu atoms as M1, M2, M3 and M4 as shown in Fig. 8(b). For the clean surface, we make full atomic relaxation of the two outermost Cu layers on each side while keeping the middle three layers fixed at their bulk values. These calculations are required to minimize numerical errors and determine accurately adsorption energies. With respect to the bulk spacing of 2.10 Å, the obtained interlayer relaxations are 0.8% between layer 1 and 2, and 0.5% between layer 2 and layer 3, which is in good agreement with experimental values (0.7% and 0.3% [43,44]). This relaxation has not change the symmetric structure of Cu(110) top surface, thus M1–O1–O2–M3 and M2–O1–O2–M4 have the same adsorption geometries and adsorption energy (0.85 eV). M1–O1–O2–M2 adsorption configuration is 0.18 eV less stable than the adsorption involving M3 or M4 site.

For the O₂/Mn(100) system, three stable adsorption configurations are found. The strongest adsorption is O1 binding into the M1 site and O1 binding to M3 site to form M1–O1–O2–M3 configuration with an adsorption energy of 1.54 eV, as shown in Fig. 8(c). The second and third stable configurations are O1 binding on two closer Mn surface atoms sites to form M2–O1–O2–M4 and M1–O1–O2–M2 structure. The adsorption energies for these two configurations are 1.32 and 1.19 eV, respectively.

For O₂ adsorption on transition metal Ni (100) surface, we found the adsorption configuration is similar with O₂ adsorption structure and orientation on transition metal Cu (100) surface. M1–O1–O2–M3 and M2–O1–O2–M4 both are the most favorable adsorption structures for O₂ molecule, and the adsorption energy is 1.26 eV. We showed the M1–O1–O2–M3 in Fig. 8(d). The second stable adsorption structure is M1–O1–O2–M2, which has an adsorption energy of 1.03 eV. Although the surface geometry of Ni(100) is similar with Cu(100), we found the adsorption energy for the most stable configuration on Ni(100) is about 0.4 eV higher than that on Cu(100) surface. Actually, from Table 1, we can see the O₂ adsorption energy on Cu surface is lower compared with that on the other transition metals, which suggests that the attraction interaction between O₂ and Cu surface is relatively weak. In summary, the adsorption energies of the four 3d metal systems follow a periodic trend, i.e., lower chemisorption energy as one proceeds from left to right in the 3d series: Mn (1.54 eV) > Co (1.44 eV) > Ni (1.26 eV) > Cu (0.85 eV), which indicates that the early transition metals tend to have stronger interaction with O₂ than the late transition metals.

We have found the O–O bond elongation upon O₂ adsorption on Co, Cu, Mn and Ni surface, which suggests electron transfer from the metal surface to the O₂ molecule. To quantify the electron transfer between the surface and O₂, a Bader analysis was carried out for four most stable O₂/metal systems as shown in Fig. 8. The results shows the adsorbed O₂ was reduced to about −0.93, −0.67, −1.12, and −0.79|e| on Co, Cu, Mn and Ni surface, respectively. Early transition metal surfaces tend to transfer more charge to the O₂ molecule than the late transition metal surface, which correlates well with the adsorption energies, i.e., the more the electron transfer for the surface to O₂, the stronger the adsorption of O₂.

3.3. O₂ dissociation and diffusion

Adsorption of O₂ is followed by breaking of the coordinated O–O bond with electron transfer. Thus, the resulting structure will be two oxygen adatoms (2O_{ad}). Oxygen adatom has higher activity compared to O₂ molecule. To build up a systematic study of oxygen atom interactions on the metal surface, we have calculated the adsorption energies of O on Co, Cu, Mn, Ni (110) surface for a range of coverages θ . We define θ as ratio of the number of adsorbed

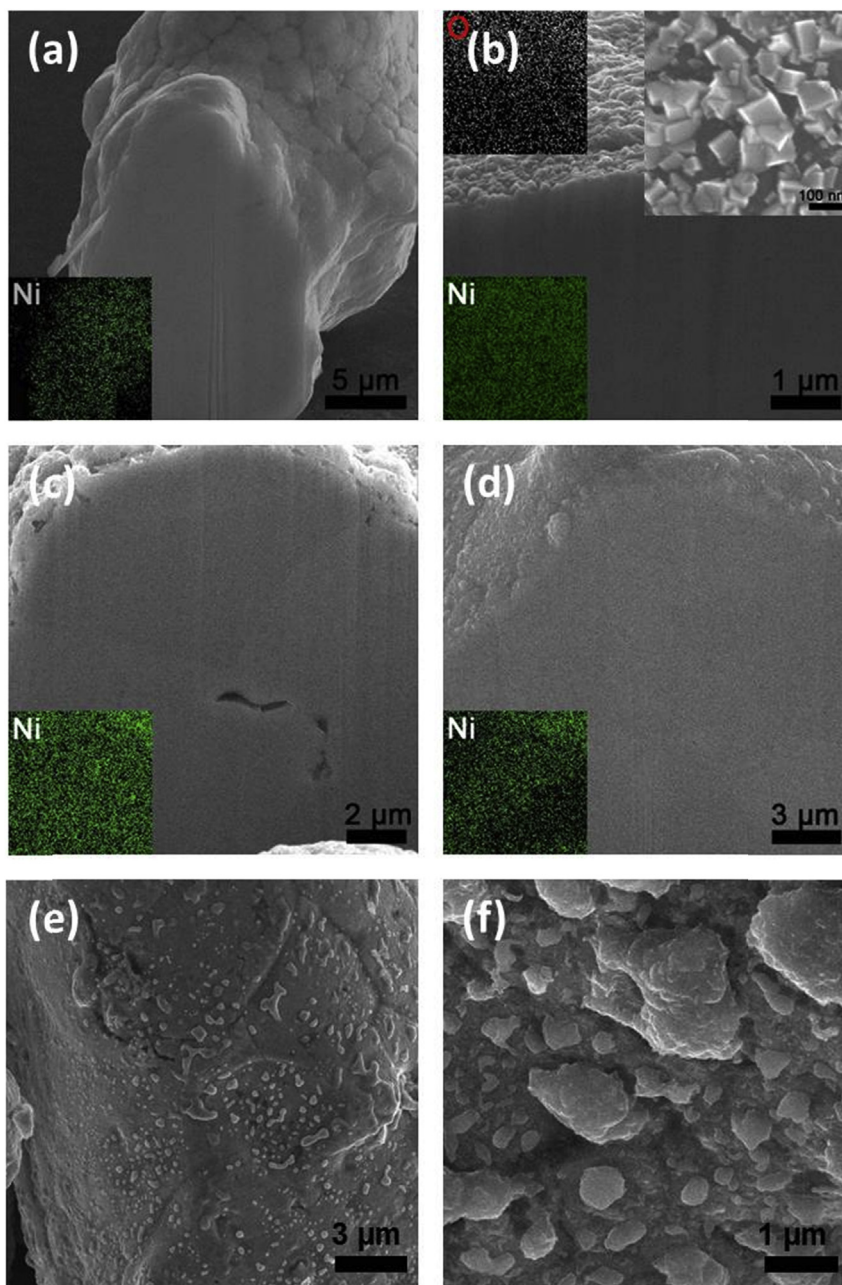


Fig. 6. SEM images of Ni microparticles (a) cross section of an initial microparticle; (b) cross section of an oxidized microparticle; (c) cross section of an microparticle after one redox reaction cycle; (d) cross section of an microparticle after five redox reaction cycles; insets: EDS mapping with blue and white representing Ni and O, respectively; (e) surface of the microparticle after one redox reaction cycle; (f) surface of the microparticle after five redox reaction cycles. (For interpretation of the references to colour in this figure legend, the reader is referred to the web version of this article.)

atoms to the number of atoms in an ideal substrate layer. For on-surface adsorption at each of these coverages, the oxygen adatoms are placed in the surface hollow site, metal-metal bridge site and metal atop sites.

The average adsorption energy per oxygen atom $E_{ad}(O)$ is calculated using the equation below:

$$E_{ad}(O) = \frac{1}{N_O} (E_M + N_O E_O - E_{O-M}) \quad (8)$$

where N_O is the number of oxygen atoms in the surface supercell. The total energies of the adsorbate-surface system, the clean transition metal surface, and the free oxygen atom are represented

by E_{O-M} , E_M , and E_O , respectively. The average adsorption energy can alternatively be referred to the dissociation energy of the O_2 molecule by subtracting half the binding energy of O_2 . The calculated average O adsorption energies are presented in Table 2.

We can see the adsorption energy of O on transition metal almost keep constant at low coverage (0.06–0.25 ML), but thereafter decreases with increasing coverage (0.25–1 ML), indicating a repulsive interaction between surface O ions. After dissociation, we found the oxygen ion binding energies on transition metal surfaces are similar when coverage is high. In addition, we found that the binding energies of O at subsurface sites change slightly when the coverage is from 0.25 to 1.00 ML, suggesting that the repulsive effect between the subsurface oxygen and the energy needed to

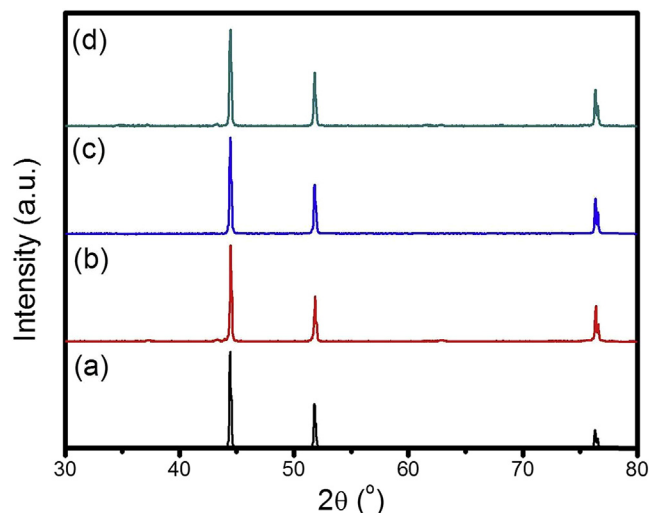


Fig. 7. XRD spectra of Ni particle. (a) Initial (b) after oxidation (c) after one redox cycle (d) after five redox cycles at 700 °C.

Table 1

Adsorption energies (in eV) of oxygen molecule on the transition metal (100) surface in different configurations.

	Co	Surface Cu	Mn	Ni
M1-O1-O2-M2	1.25	0.67	1.19	1.03
M1-O1-O2-M3	1.44	0.85	1.54	1.26
M2-O1-O2-M4	0.83	0.85	1.32	1.26

deform the transition metal lattice which usually decreases with increasing coverage interact each other.

Based on the stable adsorption structure before and after O₂ dissociation, we can explore the O₂ dissociation and initial oxygen ion diffusion process by NEB method. Vibrational frequencies were calculated to locate each transition state. For example, in the hollow dissociation path, the adsorbed O₂ molecule (M1-O1-O2-M3 configuration) migrates into hollow site, then dissociates into two oxygen ions. In this paper, we only show the most favorable dissociation and diffusion path for comparison (Fig. 9).

For the Co(100) surface, two transition states were located as

Table 2

Calculated average O adsorption energies for different coverages of O on the transition metal surfaces (eV).

	Co	Surface Cu	Mn	Ni
0.06	3.23	4.45	3.57	2.96
0.11	3.21	4.42	3.57	2.93
0.25	3.14	4.40	3.55	2.91
0.50	2.84	3.52	2.69	2.45
0.75	2.45	3.09	2.33	2.03
1.00	2.23	2.45	2.01	1.94

shown in Fig. 9. The first transition state TS1 is obtained in the dissociation of O1–O2 bond of oxygen molecule, and the second transition state TS2 was found when dissociated O ion diffusion into the subsurface to form a three-fold Co–O structure. The reaction barrier for the first transition state is 0.5 eV, suggesting Co has a high activity for O₂ dissociation. For Cu, Mn and Ni (100) surfaces, the structures of the transition states found were similar to TS1/Co system, and the barriers were calculated to be 0.85, 0.28, and 0.73 eV, respectively. Therefore, Co, Mn and Ni are more active for O₂ dissociation thus more favorable to produce O ion for redox reaction in CLC system. From Fig. 9, we also can see the oxygen ion diffusion barrier in Cu is lower than O₂ dissociation barrier, which results in that the surface lattice oxygen atoms of Cu oxide are easy to diffuse and release. It is notable that the O₂ dissociation process on Mn and Co surfaces is very exothermic, releasing 2.6 eV/O₂ of heat and 1.5 eV/O₂ of heat, respectively. Given the relative magnitudes of the adsorption energy, dissociation energy barrier and overall reaction exothermicity, adsorbed O₂ molecules will dissociate, rather than desorb, upon heating of the surface to form two chemisorbed O species. The surface relaxation and reconstruction indicate a high level of flexibility during the dissociation process, especially after the transition state. It also indicates substantial involvement of surface Mn and Co atoms in facilitating the scission of the O–O bond. For comparison, we also plot the oxygen dissociation energy profiles using the second favorable adsorption configuration as initial states as shown in Fig. 9 (dash lines). We can see the O₂ dissociation barrier for M1-O1-O2-M2 path on Co is ~0.3 eV lower than M1-O1-O2-M3 path, and M1-O1-O2-M4 path on Mn is ~0.5 eV lower than M1-O1-O2-M3 path. However, for Ni and Cu, the O₂ dissociation barriers via M1-O1-O2-M2 path and M1-O1-O2-M3 path are close.

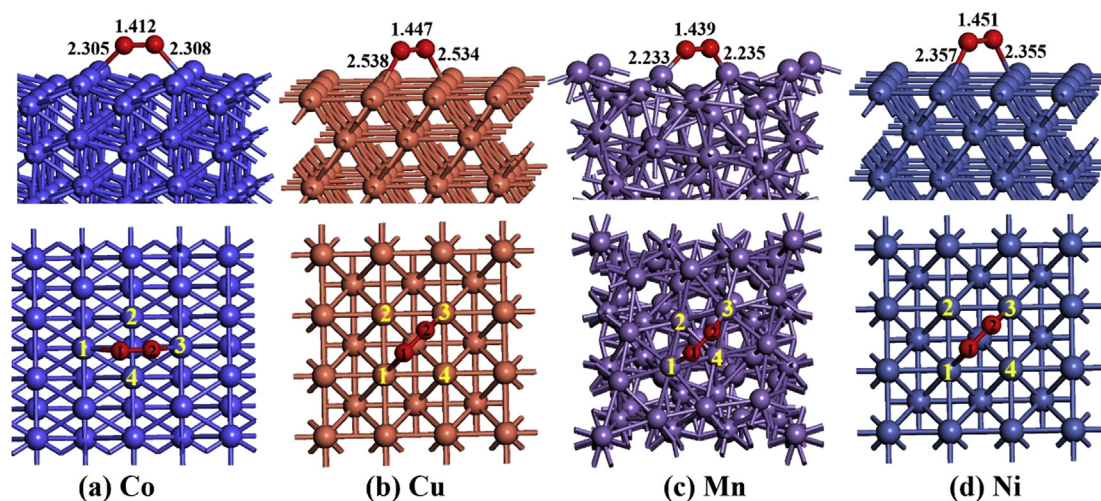


Fig. 8. The most stable adsorption structures of O₂ on transition metals (Co, Cu, Mn, Ni). The distance of O–O bond and O–metal bond are indicated (Å). Upper: side view; bottom: top view.

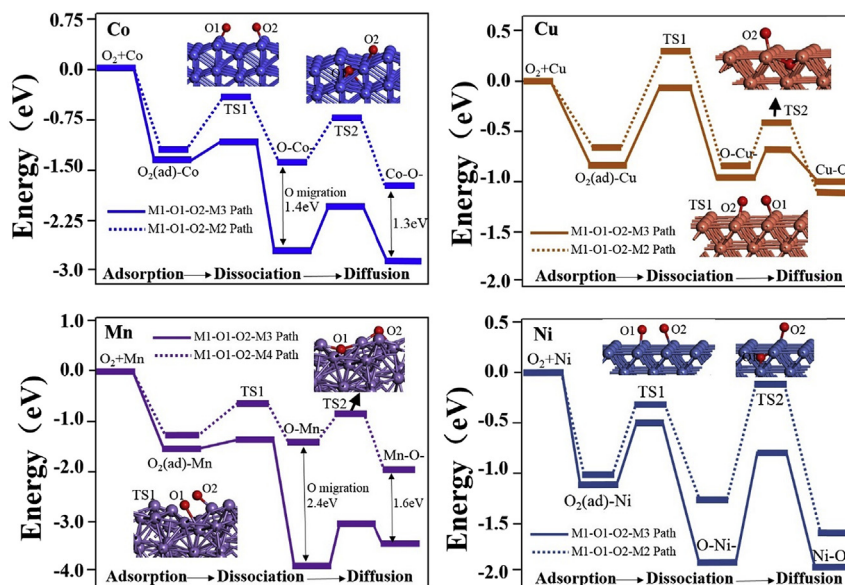


Fig. 9. Calculated reaction coordinates of O₂ dissociation and diffusion on Co, Cu, Mn and Ni (100) surfaces. The geometries of transition states are given. O–metal denotes adsorbed O ion at the surface. Metal–O– denotes the O ion has diffuse into the metal surface.

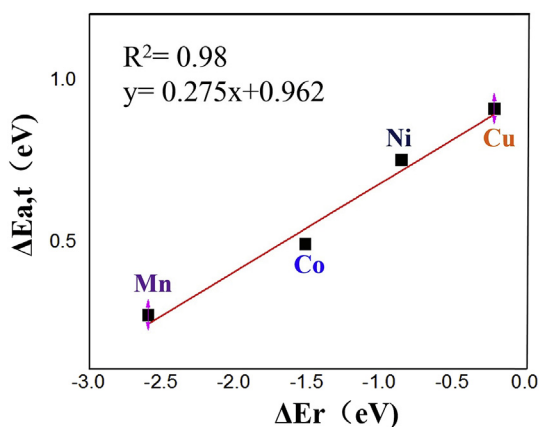


Fig. 10. Modified Brønsted–Evans–Polanyi (BEP) relationship for O–O bond scission of O₂ via the most favorable path on transition metal surfaces. Reaction barriers and reaction energies are relative to initial adsorption configuration.

In general, the reaction barriers will keep the same trend with the reaction energies. Moreover, the total reaction barriers ($\Delta E_{a,t}$) and the reaction energies ΔE_r follow a linear relationship for the O–O bond scission of O₂. The modified BEP relationship was developed as: $y = 0.275x + 0.962$ as shown in Fig. 10. This relationship is significant in estimating reaction barriers on other transition metal surfaces for the O–O bond scission of O₂.

We further analyze the O diffusion on the transition metal surfaces. In Fig. 9, we can see oxygen ion diffusion barrier for Co, Mn and Ni surfaces are relatively low ($<1\text{eV}$). However, the diffusion barrier for Ni surface are higher 1 eV, which results in lower oxygen mobility compared with Co, Mn and Ni. However, because Ni surface can be easily oxidized to NiO due to high activity of Ni for O₂ dissociation, it is necessary to investigate the oxygen vacancy formation in Ni oxide. Also, we investigate the vacancy formation in CoO, Co₃O₄, CuO, Cu₂O, MnO, Mn₃O₄ for understanding the oxygen role in the morphological evolution of these transition metal surface.

One oxygen vacancy was created in the transition metal oxide

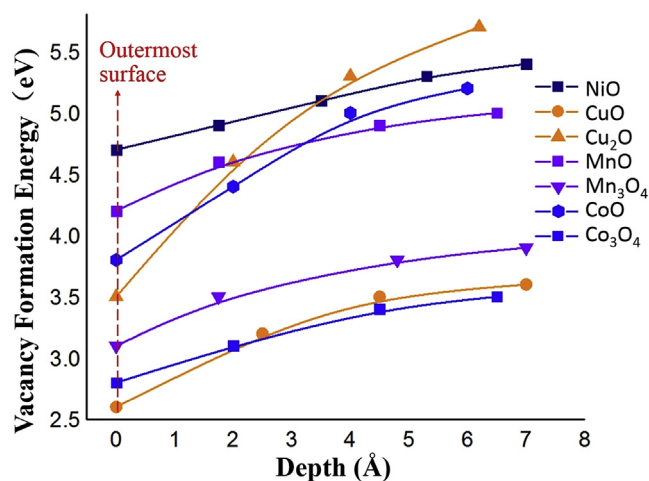


Fig. 11. Vacancy formation energy on the surface and on the subsurface as a function of depth for transition metal oxides.

slab and the vacancy formation energy with structural relaxation evaluated at depths of oxygen vacancy to the outmost surface. The vacancy formation energy on the surface and on the subsurface as a function of depth for transition metal oxides are plotted as shown in Fig. 11. From Fig. 11, we found that the formation energies increase with the depth. In the outermost surface, the oxygen vacancy formation energy is lower than 5 eV for all these transition metal oxides. For CuO, Co₃O₄ and Mn₃O₄, the vacancy formation energy is lower than 4 eV even the depth is larger than 7 Å. The low vacancy formation energy makes them feasible CLOU oxygen carrier materials.

For Cu₂O, MnO and CoO, the vacancy formation energy of larger than 4.5 eV occurs predominantly when the depth is larger than 5 Å. However, for NiO, the vacancy formation energy is higher than 4.5 eV even the vacancy is close to the outmost surface. It indicates it is unfavorable for NiO to form surface defect during redox reaction. This is consistent with SEM observation in Fig. 6(c) and (d). Therefore, to apply Ni as oxygen carrier material, it is necessary to

add suitable support which can facilitate the oxygen vacancy formation. We notice that the vacancy formation energy in higher oxidation states is lower than the lower oxidation states. The vacancy formation energy in Co_3O_4 is lower than in CoO , thus the reduction from Co_3O_4 to CoO is more energy favorable than from CoO to Co , this is consistent with our XRD results in Fig. 2. Similarly, the vacancy formation energy in CuO is lower than in Cu_2O , which suggests CuO reduction in CLOU process is more likely to result in Cu_2O rather than Cu , this explains our XRD data in Fig. 3. In Mn system, the vacancy formation energy in Mn_3O_4 is lower than in MnO , consequently MnO , instead of Mn , becomes the reducing product in chemical looping reactions, as seen in Fig. 5.

4. Conclusions

In this work, we compared the structural changes in transition metal oxide particles at a nanoscale during redox reactions, which affect their performance on a macroscopic level. This study focused on the cyclic oxidation–reduction reactions of Co , Cu , Ni and Mn systems that are transition metals used in chemical looping technology applications. Upon oxidation, dense Co microparticles converted to Co_3O_4 with the morphology changed to a porous structure. This was ascribed to processes associated with ion transport, diffusion, and volume expansion. The Co microparticles were oxidized to Co_3O_4 upon cyclic oxidation with increasing CoO impurity. CuO is desired to be reduced to Cu_2O during reduction and oxidized to CuO within technology interest. The atomistic thermodynamics methods and density functional theory calculations show Cu activity is weaker than Mn , Co and Ni . Mn microparticles were oxidized to a mixed phases of MnO and Mn_3O_4 , which causes severe delamination during oxidation. This delamination can be self-healed during reduction. Ni microparticles can promptly react with air to form NiO crystals on the surface. These crystals had very little oxygen defects due to high oxygen diffusion barrier, which leads to dense Ni surface. Consequently, Ni microparticles in CLC applications are mostly limited to surface activities. The O_2 adsorption study indicates that the early transition metals tend to have stronger interaction with O_2 than the late transition metals. Also, our modified Brønsted–Evans–Polanyi (BEP) relationship for reaction energies and total reaction barriers reveals that reactions of earlier transition metals are more exergonic and have lower oxygen dissociation barriers than those of later transition metals. In addition, it was found that for these transition metal oxides the oxygen vacancy formation energies increase with the depth. The oxide in the higher oxidation state of transition metal has lower vacancy formation energy, which can facilitate to form defective nanostructures. These findings together with the morphological changes during the redox reactions in transition metal systems provide an insight into the reaction mechanism at atomic level. They also form a fundamental basis for understanding transformations occurring during the redox process for transition metal oxide materials that are of value to metal oxide material selection and design for chemical looping applications.

Acknowledgements

The valuable support provided by the Center for Electron Microscopy and the Analysis, and NanoSystem Laboratory at The Ohio State University and by the Supercomputer Center is gratefully acknowledged.

References

- [1] L.-S. Fan, L. Zeng, S. Luo, Chemical looping technology platform, *AIChE J.* 61 (2015) 2–22.
- [2] L.-S. Fan, L. Zeng, W. Wang, S. Luo, Chemical looping processes for CO_2 capture and carbonaceous fuel conversion—prospect and opportunity, *Energy Environ. Sci.* 5 (2012) 67254–67280.
- [3] A. Lyngfelt, Oxygen carriers for chemical looping combustion –4000 h of operational experience oil gas, *Sci. Technol.* 66 (2011) 161–172.
- [4] L. Zeng, S. Luo, D. Sridhar, L.-S. Fan, Chemical looping processes—particle characterization, ionic diffusion–reaction mechanism and reactor engineering, *Rev. Chem. Eng.* 28 (2012) 1–42.
- [5] J. Adánez, L.F. de Diego, F. García-Labiano, P. Gayán, A. Abad, J.M. Palacios, Selection of oxygen carriers for chemical-looping combustion, *Energy Fuels* 18 (2004) 371–377.
- [6] T. Mattisson, H. Leion, A. Lyngfelt, Chemical-looping with oxygen uncoupling using CuO/ZrO_2 with petroleum coke, *Fuel* 88 (2009) 683–690.
- [7] F. Li, H.-R. Kim, D. Sridhar, F. Wang, L. Zeng, J. Chen, L.-S. Fan, Syngas chemical looping gasification process: oxygen carrier particle selection and performance, *Energy Fuels* 23 (2009) 4182–4189.
- [8] Lei Xu, Jianan Wang, Zhenshan Li, Ningsheng Cai, Experimental study of cement-supported CuO oxygen carriers in chemical looping with oxygen uncoupling (CLOU), *Energy Fuels* 27 (2013) 1522–1530.
- [9] Alberto Abad, Francisco García-Labiano, Luis F. de Diego, Pilar Gayán, Juan Adánez, Reduction kinetics of Cu -, Ni -, and Fe -Based oxygen carriers using syngas ($\text{CO} + \text{H}_2$) for chemical-looping combustion, *Energy Fuels* 21 (2007) 1843–1853.
- [10] E. Jerndal, T. Mattisson, A. Lyngfelt, Thermal analysis of chemical-looping combustion, *Chem. Eng. Res. Des.* A 84 (2006) 795–806.
- [11] W.K. Lewis, E.R. Gilliland, M.P. Sweeney, Gasification of carbon: metal oxides in a fluidized powder bed, *Chem. Eng. Prog.* 47 (1951) 251–256.
- [12] M. Ishida, H. Jin, A novel chemical-looping combustor without NO_x formation, *Ind. Eng. Chem. Res.* 35 (1996) 2469–2472.
- [13] H. Jin, T. Okamoto, M. Ishida, Development of a novel chemical-looping combustion: synthesis of a looping material with a double metal oxide of CoO – NiO , *Energy Fuels* 12 (1998) 1272–1277.
- [14] L. Qin, Z. Cheng, J.A. Fan, D. Kopeček, D. Xu, N. Deshpande, L.-S. Fan, Nanostructure formation mechanism and ion diffusion in iron–titanium composite materials with chemical looping redox reactions, *J. Mater. Chem. A* 3 (2015) 11302–11312.
- [15] C. Di Valentin, G. Pacchioni, A. Selloni, Electronic structure of defect states in hydroxylated and reduced rutile $\text{TiO}_2(110)$ surfaces, *Phys. Rev. Lett.* 97 (2006) 166803.
- [16] Y. Wang, D.J. Doren, First-principles calculations on TiO_2 doped by N , Nd , and vacancy, *Solid State Commun.* 136 (2005) 186.
- [17] A. Eichler, Tetragonal Y-doped zirconia: structure and ion conductivity, *Phys. Rev. B* 64 (2001) 174103.
- [18] A.A. Safonov, A.A. Bagatur'yants, A.A. Korkin, Oxygen vacancies in tetragonal ZrO_2 : Ab initio embedded cluster calculations, *Microelectron. Eng.* 69 (2003) 629.
- [19] K. Hermann, M. Witko, R. Druzinic, R. Tokarz, Oxygen vacancies at oxide surfaces: Ab initio density functional theory studies on vanadium pentoxide, *Appl. Phys. A* 72 (2001) 429.
- [20] R. Tokarz-Sobieraj, M. Witko, R. Grybos, Reduction and re-oxidation of molybdena and vanadia: DFT cluster model studies, *Catal. Today* 99 (2005) 241.
- [21] M.V. Ganduglia-Pirovano, J. Sauer, Stability of reduced $\text{V}_2\text{O}_5(001)$ surfaces, *Phys. Rev. B* 70 (2004) 045422.
- [22] T.X.T. Sayle, S.C. Parker, C.R.A. Catlow, The role of oxygen vacancies on ceria surfaces in the oxidation of carbon-monoxide, *Surf. Sci.* 316 (1994) 329.
- [23] Z. Cheng, B. Sherman, C. Lo, Carbon dioxide adsorption and activation on Ceria (110), *J. Chem. Phys.* 138 (2013) 014702.
- [24] Z. Cheng, C. Lo, Effect of support structure and composition on the catalytic activity of Pt nanoclusters for methane dehydrogenation, *Ind. Eng. Chem. Res.* 52 (2013) 15447–15454.
- [25] M. Nolan, J.E. Fearon, G.W. Watson, Oxygen vacancy formation and migration in ceria, *Solid State Ion.* 177 (2006) 3069.
- [26] G. Kresse, J. Hafner, Ab initio molecular dynamics for liquid metals, *Phys. Rev. B* 47 (1993) 558–561.
- [27] G. Kresse, J. Furthmüller, Efficiency of ab-initio total energy calculations for metals and semiconductors using a plane-wave basis set, *J. Comput. Mater. Sci.* 6 (1996) 15–50.
- [28] G. Kresse, J. Furthmüller, Efficient iterative schemes for ab initio total-energy calculations using a plane-wave basis set, *Phys. Rev. B* 54 (1996) 11169–11186.
- [29] J.P. Perdew, K. Burke, M. Ernzerhof, Generalized gradient approximation made simple, *Phys. Rev. Lett.* 77 (1996) 3865–3868.
- [30] P.E. Blöchl, Projector augmented-wave method, *Phys. Rev. B* 50 (1994) 17953–17979.
- [31] G. Kresse, D. Joubert, From ultrasoft pseudopotentials to the projector augmented-wave method, *Phys. Rev. B* 59 (1999) 1758–1775.
- [32] P.E. Blöchl, O. Jepsen, O.K. Anderson, Improved tetrahedron method for Brillouin-zone integrations, *Phys. Rev. B* 49 (1994) 16223–16233.
- [33] K. Huber, G. Herzberg, *Molecular Spectra and Molecular Structure IV: Constants of Diatomic Molecules*, Van Nostrand Reinhold, New York, 1979.
- [34] D. Sheppard, G. Henkelman, Paths to which the nudged elastic band converges, *J. Comput. Chem.* 32 (2011) 1769–1771.
- [35] G. Henkelman, B.P. Uberuaga, H.J. Jónsson, A climbing image nudged elastic band method for finding saddle points and minimum energy paths, *J. Chem.*

- Phys. 113 (2000) 9901–9904.
- [36] Z. Cheng, C.S. Lo, Propagation of olefin metathesis to propene on WO_3 catalysts: a mechanistic and kinetic study, *ACS Catal.* 5 (2015) 59–72.
- [37] Z. Cheng, C. Lo, Mechanistic and microkinetic analysis of CO_2 hydrogenation on ceria, *Phys. Chem. Chem. Phys.* 18 (2016) 7987–7996.
- [38] L. Qin, A. Majumder, J.A. Fan, D. Kopeček, L.-S. Fan, Evolution of nanoscale morphology in single and binary metal oxide microparticles during reduction and oxidation processes, *J. Mater. Chem. A* 2 (2014) 17511–17520.
- [39] Z. Cheng, L. Qin, M. Guo, J.A. Fan, D. Xu, L.-S. Fan, Methane adsorption and dissociation on iron oxide oxygen carrier: role of oxygen vacancy, *Phys. Chem. Chem. Phys.* 18 (2016) 16423–16435.
- [40] J. Darul, C. Lathe, P. Piszora, Mn_3O_4 under high pressure and temperature: thermal stability, polymorphism, and elastic properties, *J. Phys. Chem. C* 117 (2013) 23487–23494.
- [41] M. Mori, Irreversible expansion behavior of $\text{Mn}_3\text{O}_{4+\delta}$ spinel and shrinkage behavior of $\text{La}_{0.6}\text{Sr}_{0.4}\text{MnO}_3$ composites with the spinel during thermal cycling in O_2 atmosphere, *J. Electrochem. Soc.* 149 (2002) A995–A1000.
- [42] I. Suzuki, S. Okajima, K. Seya, Thermal expansion of single-crystal manganosite, *J. Phys. Earth* 27 (1979) 63–69.
- [43] S.A. Lindgren, L. Walldén, J. Rundgren, P. Westrin, Low-energy electron diffraction from $\text{Cu}(111)$: subthreshold effect and energy-dependent inner potential; surface relaxation and metric distances between spectra, *Phys. Rev. B* 29 (1984) 576–588.
- [44] S.P. Tear, K. Röhl, M. Prutton, A comparison of reliability (R) factors in a LEED structural analysis of the copper (111) surface, *J. Phys. C Solid State Phys.* 14 (1981) 3297–3311.